Nonparallelism attributes and data adaptive Kuwahara image processing

Jie Qi, and Kurt Marfurt, The University of Oklahoma.*

Summary

To map the properties of seismic facies, we introduce 3D nonparallelism attributes that highlight lateral variation of parallelism of reflectors and their energy. The nonparallelism attributes provide quantitative measures of reflector dips by extracting statistical components of the 3D seismic amplitude volume. Many seismic attributes computed by a fixed window, exhibit a "salt and pepper" classification, which is more often seen on karst collapse features, salt dome, and mass transport complex facies. In our workflow, we also propose a 3D structure-oriented adaptive Kuwahara filtering technique to precondition seismic attributes for subsequent machine learning classification. The new adaptive Kuwahara filtering method is more efficient than the original 3D Kuwahara filtering to increase facies discrimination of seismic attributes. We validate the statistic measure of reflector dips and statistic measure of seismic spectrum to map karst collapse facies.

Introduction

Dip attribute, measured reflector dipping angle, is significant to differentiate one complex deposition facies from surrounding facies. When asked "which dip is useful for machine learning in differentiating seismic facies?", it could be some kind of continuity dip measurement rather than a specific dip or a dip component. The first statistical measurement of reflector dips was first proposed by Barnes (2003) and measures "parallelism" (or more precisely, deviation from parallelism) which is estimate by the standard deviation of vector dip. Reflector convergence and reflector rotation are also the statistic measures of structure (Marfurt and Rich, 2010). Lateral changes in reflector dips can be measured by curvature or aberrancy, while vertical changes in dips are measured by reflector convergence. In both cases, the strength of these anomalies rather than their strike or azimuth is the differentiating factor.

Another kind of seismic attributes in seismic facies analysis is the amplitude attribute, which measure the magnitude or strength of reflectors in seismic amplitude volumes. Derivative approaches to measure amplitude variability are mean amplitude, root mean square (RMS) amplitude, and average amplitude. By Employing Hilbert Transform, one can compute instantaneous envelope and frequency, amplitude volume transform, and other complex trace amplitude attributes to measure amplitude vertical variation. For measuring lateral variation of amplitude, an alternative approach is to compute amplitude gradient along inline- and crossline-axis. When asked "which amplitude is useful for machine learning", it could be the amplitude attribute that can exhibit either sharp edges of different facies, or strong amplitude contrast between each facies. Qi et al. (2014) found that the coherent amplitude gradients and its second derivatives of the coherent amplitude gradient are sensitive to subtle lateral amplitude discontinuities such as small (less than 1/4 wavelength) karst collapse features, and joints.

3D image process filters are promising for lateral resolution improvement of seismic attributes. For seismic attribute image processing, Al-Dossary and Marfurt (2007) proposed a multistage median filter and compare with other statistic filters through noise rejection of curvature attributes. Qi et al. (2016) employed a structure-oriented Kuwahara filter to smooth interior textures and sharpen edges of coherence, and GLCM texture attribute images, which showed advanced classification with the Kuwahara filtered attribute rather than unfiltered attributes.

Although there are many seismic facies classification techniques, instead of comparing which algorithms are better, in this paper we focus on the input attributes that are significant to improve facies classification. We implement data adaptive Kuwahara filtering to nonparallelism attributes in order to smooth interior materials of facies that gives rise to "blocked" facies. The filter also results in sharpen boundaries of different facies and increased resolution of facies analysis. We validate our new attribute by applying those attributes to a machine learning algorithm on real seismic datasets.

Statistical measurements of structure dip and energy gradient vectors

Let's assume we have a volumetric estimate of dip in inline direction (x-axis), p, and crossline direction (y-axis), q, which are given as:

$$p = \frac{\partial t}{\partial x}, \tag{1}$$

and

$$q = \frac{\partial t}{\partial y}, \tag{2}$$

Then, in a J-sample analysis window, we can find the energy weighted (e.g. total energy, e) standard deviation of vector dip about its mean to be:

$$\sigma_{dip} = \left\{ \frac{\sum_{j=1}^{J} e_j [(p_j - \mu)(p_j - \mu) + (q_j - v)(q_j - v)]}{\sum_{j=1}^{J} e_j} \right\}^{1/2}, \tag{3}$$

where the weighted mean values are:

$$\mu = \frac{\sum_{j=1}^{J} e_j p_j}{\sum_{j=1}^{J} e_j}, \tag{4}$$

and

$$v = \frac{\sum_{j=1}^{J} e_j q_j}{\sum_{j=1}^{J} e_j}. \tag{5}$$

10.1190/segam2019-3216022.1

The energy gradient measures the lateral variation in seismic energy (or alternatively RMS amplitude) along structural dip. For relatively conformal reflectors, the energy gradient is often a measure of thinning or thickening, or of the lateral change in impedance contrast between strata. We wish to differentiate such "organized" lateral changes in energy from chaotic changes, such as seen within salt domes, karst collapse, gas chimneys, overpressured shales, and some areas of mass transport deposits. In this case, we will not weight the results. The energy deviation of volumetric estimate of inline energy gradient, g, and crossline energy gradient, h, is:

$$\varepsilon_e = \sum_{j=1}^{J}\left[(g_j-\bar{g})(g_j-\bar{g})+(h_j-\bar{h})(h_j-\bar{h})\right], \quad (6)$$

where $\overline{g}=\frac{1}{J}\sum_{j=1}^{J} g_j$, and $\overline{h}=\frac{1}{J}\sum_{j=1}^{J} h_j$ are the statistical mean of inline energy gradient, g, and crossline energy gradient, h. Then, the covariance of vector dip and energy C_{cov} can be defined as:

$$C_{cov}=\left\{\frac{\sum_{j=1}^{J}\left\{\left[e_j\bar{n}(p_j-\mu)(g_j-\bar{g})\right]^2+e_j\bar{n}(q_j-v)(h_j-\bar{h})\right\}^2}{\sum_{j=1}^{J} e_j}\right\}, \quad (7)$$

where vector $\overline{n}$ is the normal vector of dip vectors and shown as:

$$\bar{n}_j=\left[\frac{1}{(p_j-\bar{p})(q_j-\bar{q})+1}\right]^{1/2}, \quad (8)$$

where $\overline{p}$ and $\overline{q}$ is the statistical mean of vector dips p and q. Equation 3, 6, and 7 are the nonparallelism attributes, which measure reflector's both nonparallelism and strength along structure dips. Because of subtraction of energy-weighted mean, the deviation of vector dip (Equation 3) rather than coherence or the GLCM texture attributes, is more sensitive to the reflectors that are compacted closely or combined with chaotic reflections. The deviation of volumetric energy gradient indicates lateral variation of seismic amplitude, while the covariance of vector dip and energy gradient highlights deformed reflectors that are chaotic, high amplitude, and rotated. Among these three attributes, the deviation of vector dip and energy exhibits.

Data Adaptive Kuwahara Image Processing

When used for seismic facies analysis, the fixed window Kuwahara window size needed for one facies may be inappropriate for a second facies. Likewise, as seismic resolution decreases with depth, a fixed window size may oversmooth shallow features and undersmooth deeper features. To address this shortcoming, we modify the analysis window of the 3D structure-oriented Kuwahara filter to be adaptive along lateral and vertical axes. Lin et al. (2014) used an adaptive window for coherence computation that define both the lateral and vertical size of the analysis window based on smoothed peak frequency. The traditional 5×5×5-voxel 3D Kuwahara filter searches 27 overlapping sub-windows and applies the median m in the overlapping window that has the smallest mean-normalized standard deviation σ/μ.

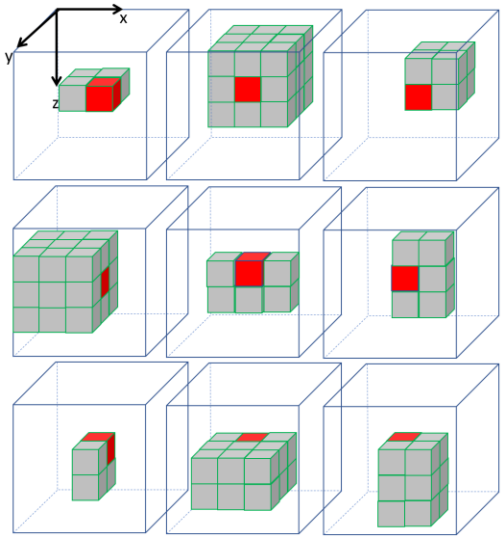

Figure 1. Cartoon of 3D adaptive Kuwahara filtering. The 5×5×5 or 125-sample analysis window is centered about the red voxel. The cartoon shows only nine of the 3×3×3 or 27 sub-windows that contain the red cube. The size of sub-window is adaptive, and increases in size with decreasing seismic resolution, defined by the local frequency of the seismic amplitude. The output is the median of the sub-window that has the smallest mean-normalized standard deviation.

We follow Lin et al. (2014) and Qi et al. (2015), and define the size of the adaptive Kuwahara searching window by the smoothed average power spectrum at each voxel. The average power spectrum is

$$P_{avg}(t,f)=\frac{1}{J(2I+1)}\sum_{j=1}^{J}\sum_{i=-I}^{I} u_j^2(t+i\Delta t,f), \quad (9)$$

where t is time sample, I is half length of the vertical analysis window, and u_j is the spectral magnitude of the j^{th} trace. The average power spectrum is averaged over all traces and $2I$+1 vertical samples. The peak frequency at time t is the frequency at which is associated with the maximum power spectrum. The resolution of spectrally balanced data is determined not only by the peak frequency, but also by the highest useable frequency. Suppose that the average power spectrum of the analysis points with its H neighboring voxels is f, first of all, we need to define the reference frequency f_{ref} of the adaptive analysis window at a given time t:

$$f_{ref}(t)=f_p(t)-\frac{\left(\sum_{f=1}^{F_p} P_{avg}(t,f)-p\sum_{f=1}^{F} P_{avg}(t,f)\right)}{P_{avg}(t,F_p)}\Delta f, \quad (10)$$

where p is a percentile of the average power spectrum (in our work P=70%), f_P is the corresponding frequency. Δf is the frequency increment between analysis window sizes in the computation of the average time-variant power spectrum. Then, the window height ΔT of the adaptive analysis window at a given time t can be defined as

10.1190/segam2019-3216022.1

$$\Delta T(t) = \frac{bP}{2f_{ref}(t)}, \quad (11)$$

Parameter $b=0.01$ is a fixed pre whitening factor. Using a reference velocity, $v(t)$, the two-way travel time window height ΔT corresponds to a spatial vertical height ΔZ,

$$\Delta Z(t) = v(t)\frac{\Delta T(t)}{2}, \quad (12)$$

Figure 1 shows a cartoon of Kuwahara overlapping windows containing the red analysis point. In each window we compute the median m, the mean μ, and the standard deviation σ. The result of the Kuwahara searching window w_l at an analysis point t is:

$$d = Arg\left(\min_{d\in\{w_l|l\in 1,2,3\ldots L\}}\left(\frac{\sigma_d}{\mu_d}\right)\right). \quad (13)$$

Thus, the filtered attribute will be the value of m_d associated with the window having the minimum value of normalized standard deviation $\frac{\sigma_d}{\mu_d}$.

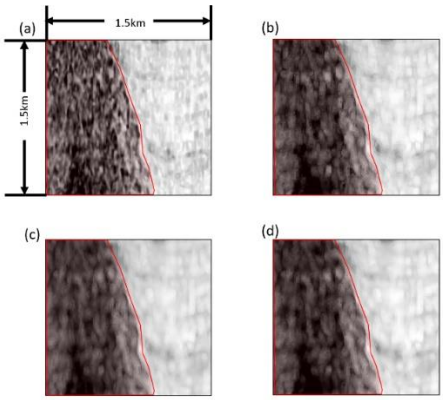

Figure 2. Cropped vertical slices through the deviation of vector dip attribute, (a) before Kuwahara filtering, (b) after 3D Kuwahara filtering with a fixed 3×3×3 analysis window, (c) after 3D Kuwahara filtering with a fixed 5×5×5 analysis window, and (d) after adaptive Kuwahara filtering where the window size varies between 3×3×3 and 5×5×5.

The 3D structure-oriented adaptive Kuwahara filter searches all windows containing a given voxel. The filtered attribute will have a smoothed facies that is shown as a blurred internal texture, and sharpened edges between each facies. The smoothness is defined by local average spectrum. The result of 3D adaptive Kuwahara filtering may somewhere look like the result of the fixed-window Kuwahara filtering computed with a large analysis window. However, one of the advantages is that the computation cost of the adaptive window is less than a large fixed window, because not any sub-windows should be equally large.

Figure 2 shows an example of application of the 3D adaptive Kuwahara filter to the deviation of vector dip in chaotic features delineation. We first apply the original 3D Kuwahara filtering results computed with a fixed 3×3×3 analysis window, which is shown in Figure 2b. Note that red polygon indicates chaotic features, and the write color texture indicate another feature. Kuwahara filtering smooths the internal details of each features and also sharpens the boundary. Figure 2c shows the original 3D Kuwahara filtering result computed with a fixed 5×5×5 analysis window, and Figure 2d shows the result of our 3D adaptive Kuwahara filter. Note that, the original Kuwahara filtering with a large window results in a better internal material, but a blurred edge. However, because using adaptive windows defined by local average spectrum, the new adaptive Kuwahara filtering not only smooths low frequency internal textures of chaotic features, but also sharpens high frequency and energy chaotic feature boundaries.

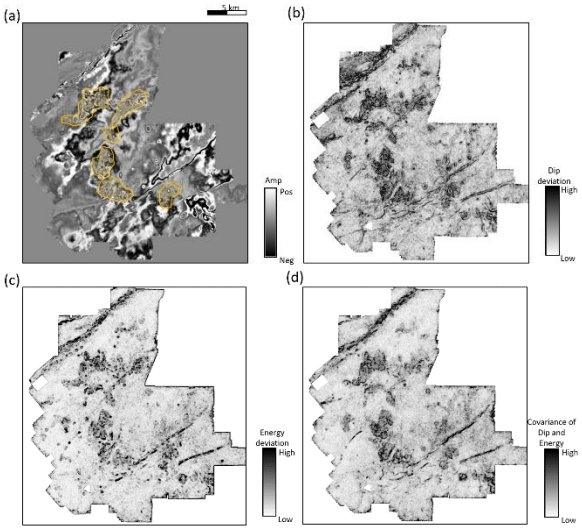

Figure 3. Time slices at t = 0.72 s through (a) the seismic amplitude volume, (b) dip deviation, (c) energy deviation, and (d) covariance of dip and energy, mapping karst collapse features on Fort Worth Basin. Note yellow polygons indicate karst collapse features that are also painted facies of interest for this dataset.

Application

Our test dataset was acquired from the Fort Worth Basin by using 16 live receiver lines forming a wide-azimuth survey. The dataset was time migrated with a 55× 55 ft bin size to image the Barnett Shale and the underlying Ellenburger carbonate formation, which is characterized by karst and solution collapse features. Figure 3a shows the time slice through the seismic amplitude volume, where carbonate is the dominant formation.

Figure 3b-3d show the proposed three nonparallelism attributes. The deviation of vector dip exhibits karst edges and reflector flexures between the layers of Barnett Shale and Ellenburger formation. The deviation of energy gradient highlights high energy collapse features and small karst

10.1190/segam2019-3216022.1

features, which of size is smaller than ¼ wavelength and showing as scatter lighting dots on Figure 3b. The covariance of vector dip and energy exhibits incoherent karst edges and faults that are like anomalies in coherence. Figure 4 shows the nonparallelism attributes after the 3D structure-oriented adaptive filtering. Note that the karst collapse facies is piecewise smoothed. Compared with original attributes, the contract between karst facies and carbonate facies is also increased. Figure 5a shows the generative topographic mapping (GTM) classification of karst collapse with nonparallelism attributes, and spectral bandwidth, GLCM entropy, GLCM variance, spectral roughness, as input. Figure 5b shows the GTM classification with the same attributes but after adaptive Kuwahara filtering. Note that Figure 5b better exhibits karst facies than Figure 5a, which is much easier for automatic computer segmentation. Figure 6 shows the karst collapse probability volume computed from the workflow proposed by Qi et al. (2016).

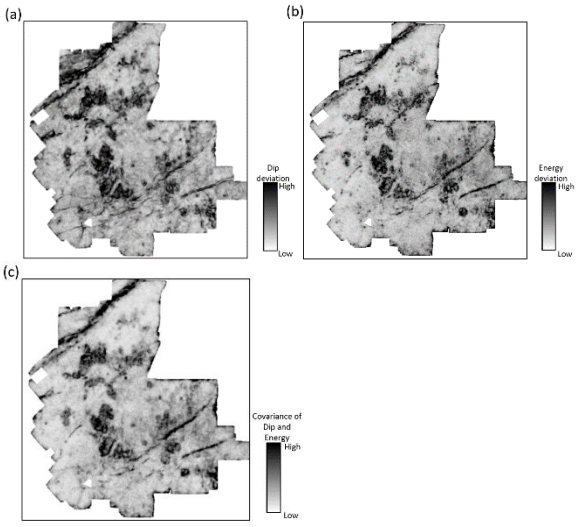

Figure 4. Time slices at t = 0.72 s through (a) dip deviation, (b) energy deviation, and (c) covariance of dip and energy after the adaptive Kuwahara filtering. Note the Kuwahara filtering smooth increases discrimination between karst collapse facies and other conformal facies.

Conclusions

Not like human interpreters, the computer can detect facies edges by fewer voxels. Thus, if there are not sharp edges or "salt and pepper" anomalies exist on facies edge, the accuracy of computer-assisted classification will be very low. We therefore propose the nonparallelism attributes and implement 3D structure-oriented adaptive Kuwahara filter to smooth interior seismic facies and sharpen edges. The adaptive Kuwahara filtering technique performs better than the original 3D Kuwahara filter by adjusting the size of sub-windows for an analysis window, which reduces the computation cost and results in sharper edges at reflections with a high frequency band such as karst edges, and smoother interior at reflections with a low frequency band such as chaotic materials. The GTM with the Kuwahara filtered attributes allows to cluster facies of interest.

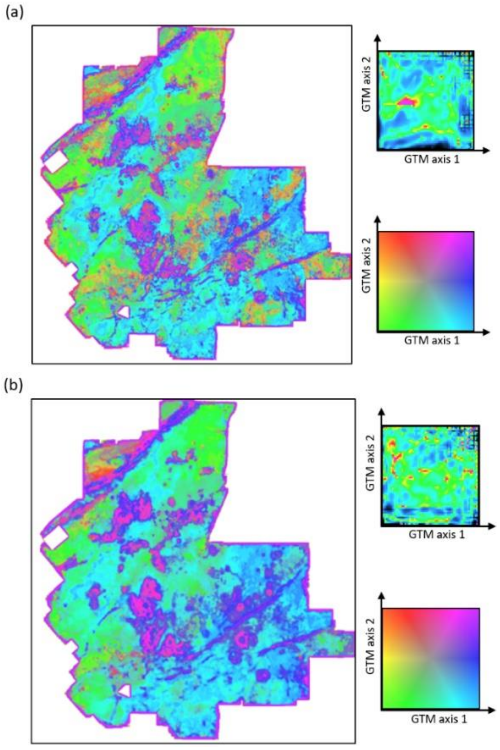

Figure 5. Time slices at t = 0.72 s through (a) the GTM classification with the attributes as input before Kuwahara filtering, and (b) the GTM classification with the adaptive Kuwahara filtered attributes as input. Note the GTM classification with the adaptive Kuwahara filtered attributes as input exhibits clearer and smoother karst collapse facies.

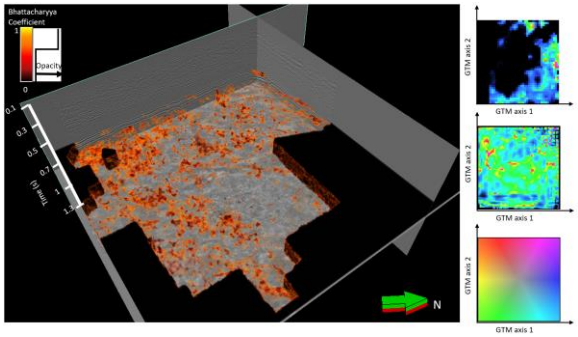

Figure 6. 3D karst collapse probability volume co-rendered with seismic amplitude computed through the workflow (Qi et al., 2016)

10.1190/segam2019-3216022.1

REFERENCES

Al-Dossary, S., and K. J. Marfurt, 2007, Lineament-preserving filtering: Geophysics, **72**, no. 1, P1–P8, doi: https://doi.org/10.1190/1.2387138.

Barnes, A. E., 2003, Shaded relief seismic attribute: Geophysics, **68**, 1281–1285, doi: https://doi.org/10.1190/1.1598120.

Lin, T., B. Zhang, S. Zhan, Z. Wan, F. Li, H. Zhou, and K. J. Marfurt, 2014, Seismic attributes of time- vs. depth-migrated data using self-adaptive window: 84th Annual International Meeting, SEG, Extended Abstracts, 1659–1662, doi: https://doi.org/10.1190/segam2014-1579.1.

Marfurt, K. J., and J. R. Rich, 2010, Beyond curvature — Volumetric estimates of reflector rotation and convergence: 80th Annual International Meeting, SEG, Expanded Abstracts, 1467–1472, doi: https://doi.org/10.1190/1.3513118.

Qi, J., M. Cahoj, A. AlAli, L. Li, and K. Marfurt, 2015, Segmentation of salt domes, mass transport complexes on 3D seismic data volumes using Kuwahara windows and multiattribute cluster analysis: 85th Annual International Meeting, SEG, Expanded Abstracts, 1821–1825, doi: https://doi.org/10.1190/segam2015-5876831.1.

Qi, J., T. Lin, T. Zhao, F. Li, and K. J. Marfurt, 2016, Semisupervised multiattribute seismic facies analysis: Interpretation, **4**, no. 1, SB91–SB106, doi: https://doi.org/10.1190/INT-2015-0098.1.

Qi, J., B. Zhang, H. Zhou, and K. J. Marfurt, 2014, Attribute expression of fault-controlled karst — Fort Worth Basin, Texas: A tutorial: Interpretation, **2**, no. 3, SF91–SF110, doi: https://doi.org/10.1190/INT-2013-0188.1.